A Qubit with Simultaneously Maximized Speed and Coherence

Miguel J. Carballido,[1,*] Simon Svab,[1] Rafael S. Eggli,[1] Taras Patlatiuk,[1] Pierre Chevalier Kwon,[1] Jonas Schuff,[2] Rahel M. Kaiser,[1] Leon C. Camenzind,[1,†] Ang Li,[3,‡] Natalia Ares,[4] Erik P.A.M Bakkers,[3] Stefano Bosco,[1,§] J. Carlos Egues,[1,5] Daniel Loss,[1,6] and Dominik M. Zumbühl[1,¶]

[1]*Department of Physics, University of Basel, Klingelbergstrasse 82, CH-4056 Basel, Switzerland*
[2]*Department of Materials, University of Oxford, Oxford OX1 3PH, United Kingdom*
[3]*Department of Applied Physics, TU Eindhoven, Den Dolech 2, 5612 AZ Eindhoven, The Netherlands*
[4]*Department of Engineering Science, University of Oxford, Oxford OX1 3PJ, United Kingdom*
[5]*Instituto de Física de São Carlos, Universidade de São Paulo, 13560-970 São Carlos, São Paulo, Brazil*
[6]*CEMS, RIKEN, Wako, Saitama 351-0198, Japan*

(Dated: February 13, 2024)

To overcome the threshold for fault-tolerant quantum computation, qubits have to be protected from their noisy environment to attain the necessary high fidelities [1, 2]. Recent experiments discovered sweet spots [3–6] with strongly enhanced coherence. However, decoupling a qubit from its surroundings also limits the control over the qubit's state [7, 8], typically leading to either coherent but slow [9, 10] or fast but short-lived [7, 11–13] qubits. This trade-off appears to be a severe fundamental limitation hampering the performance of qubits. Here, we show how this can be circumvented by demonstrating a simultaneously fast and coherent tunable regime in a hole spin qubit. In this regime, we can triple the operation speed, while simultaneously quadrupling the coherence time when tuning a local electric field, demonstrating that the qubit speed and coherence scale together without compromise. This relies on strong, quasi 1D confinement providing a local maximum in drive strength, where charge fluctuations are decoupled and thus the coherence is enhanced, yet the drive speed is maximal. A Ge/Si core/shell nanowire, operated at 1.5 K [14–17], provides the strong confinement. The driving mechanism here is the strong and tunable direct Rashba spin-orbit interaction [18–22], achieving a maximal strength at finite electrical field due to gate-dependent heavy-hole light-hole mixing. Breaking the speed-coherence trade-off makes it possible to boost fidelity and speed of one- and two-qubit gates. This concept can be expanded to planar arrays of hole or electron spin qubits as well. In this regime, the coupling to a microwave resonator is also predicted to be both strong and coherent [23, 24]. Altogether, this is opening a new path towards fault-tolerant quantum computation.

Main

Spins in semiconductor quantum dots (QD) have emerged as one of the leading contenders for encoding and processing quantum information [25–27]. Their success is attributed to their competitive coherence times [1, 28] , the demonstration of robust multi-qubit operations [29, 30], coherent spin control above 1 K [14–17] and their compatibility with industrial fabrication techniques [31–33].

Among the various semiconductor systems capable of hosting spin qubits, material systems exhibiting strong, intrinsic spin-orbit interactions (SOI), have received increasing attention in recent years [34, 35]. Taking advantage of the SOI, all-electrical spin driving can be implemented via electric dipole spin resonance (EDSR), without the requirement for on-chip micro magnets or microwave antennas. While SOI mediated EDSR allows for compact device architectures [36, 37], it has more importantly led to ultrafast Rabi oscillations ranging from 80 MHz in electrons [8], to several 100 MHz [7] and even up to 1.2 GHz [13] in holes, alas, at the expense of coherence. These remarkable observations have thus raised a pivotal concern for the future of spin qubits with strong SOI [21]: Do strong couplings to the qubit driving field inevitably lead to increased decoherence due to enhanced couplings with undesired noise sources [38]?

First steps towards reducing the coupling to charge noise have been taken via the modification of global system parameters such as the external magnetic field orientation [3–5], however, the fundamental trade-off between speed and coherence has so far prevailed.

Here we provide first experimental evidence for compromise-free scaling, through the demonstration of a coherence sweet spot that coincides with maximal Rabi driving speeds. Our observations are in agreement with previous theoretical predictions on group IV hole spin qubits [6, 21, 22, 39, 40]. Additionally, we achieve this Fast and Coherent Tunable Operating Regime (*FACTOR*) all-electrically, by controlling static gate voltages at the individual qubit level. Such local optimizations allow us to respond to the variable electrostatic environments that each qubit experiences, which can be comprised of electric stray fields from neighbouring gates or non-uniform strain.

Realising a compromise-free qubit requires navigating the intricate interplay between the tuning parameter, driving mechanism and decoherence channel. Remarkably, certain systems naturally exhibit the conditions for a *FACTOR*, such as hole spins in quasi 1D systems with strong SOI. In these systems, the g-tensors often display a high level of anisotropy, which can be notably influenced by electric fields.

* miguel.carballido@unibas.ch
† Currently at: CEMS, RIKEN, Wako, Saitama 351-0198, Japan
‡ Currently at: Institute of Microstructure and Properties of Advanced materials, Beijing University of Technology, Beijing, 100124, China
§ Currently at: QuTech and Kavli Institute of Nanoscience, Delft University of Technology, Delft, The Netherlands
¶ dominik.zumbuhl@unibas.ch

Consequently, random charge fluctuations couple to the qubit energy, resulting in reduced coherence [2]. In order to mitigate this issue, configurations with vanishing derivatives of the g-factor, with respect to voltage changes, are most promising, as they indicate a reduced coupling of g to charge noise. To realise such a sweet spot, we exploit the properties of a spin qubit hosted inside a squeezed, elongated hole quantum dot, subject to strong SOI, as is naturally provided by the geometry of a Ge/Si core/shell nanowire (NW) [7].

In such structures, the strong biaxial confinement causes heavy- and light-hole (HH-LH) states to intermix, giving rise to a strong and electrically tunable direct-Rashba spin-orbit interaction (DRSOI) [18, 19]. At an optimal HH-LH mixture, the spin-orbit strength is expected to reach a maximum as a function of an externally applied electric field. In the presence of strong SOI, when the spin-orbit length l_{SO} becomes comparable to the dot size l_{dot}, the g-factor is reduced [18–20, 41]. This gives rise to a minimum in g at the point where SOI reaches a maximum. This minimum in g as a function of electric field corresponds to the coherence sweet spot. By additionally employing iso-Zeeman EDSR driving of the qubit [42], the Rabi frequency f_R can be maximised at this very same spot. This ensures an operating regime where the qubit is both fast and long lived without compromising speed or coherence, thus defining our *FACTOR*.

Coherent Spin Control at 1.5 K

We first demonstrate the operation of our Ge/Si NW hole spin qubit at 1.5 K, adding it to the list of previously demonstrated hot qubits [14–17]. A scanning electron micrograph showing a representative device is presented in Fig. 1a. The device consists of a Ge/Si core/shell NW lying on top of nine bottom gates. For details on the device fabrication we refer to the materials and methods section. By applying positive voltages to the first five bottom gates from the left, the intrinsic hole gas inside the NW is depleted to form a hole double quantum dot (DQD) [43] with a net-effective hole occupation (m, n) on the left and right dot. The true total hole occupation has been estimated to be in the range of several dozen [41, 43, 44].

The device is operated at a net-effective charge-transition from $(1, 1)$ to $(2, 0)$ that exhibits Pauli spin blockade (PSB). We apply a positive bias across the NW and measure the current through the DQD, which provides spin to charge conversion due to PSB. This allows to read out the state of the effective spin-1/2 system, as shown in Fig. 1b. The characteristic DC transport signature of PSB can be seen in Fig. 1c, where the baseline of the bias triangle disappears in the absence of magnetic field (inset 1c).

In our setup, the right plunger gate RP, coloured in magenta in Fig. 1a, is connected to a high frequency line via a bias-tee. This allows for the application of square voltage pulses and microwave bursts to the gate, in addition to DC voltages. The measurements were performed employing a common two-stage pulsing protocol [7, 11, 16, 45], as schematically shown in Fig. 1d.

The system is initialized in a spin-blockaded effective (1,1) triplet state, by employing a specific plunger gate voltage V_{RP}, represented by the magenta stars in Figs. 1c and d.

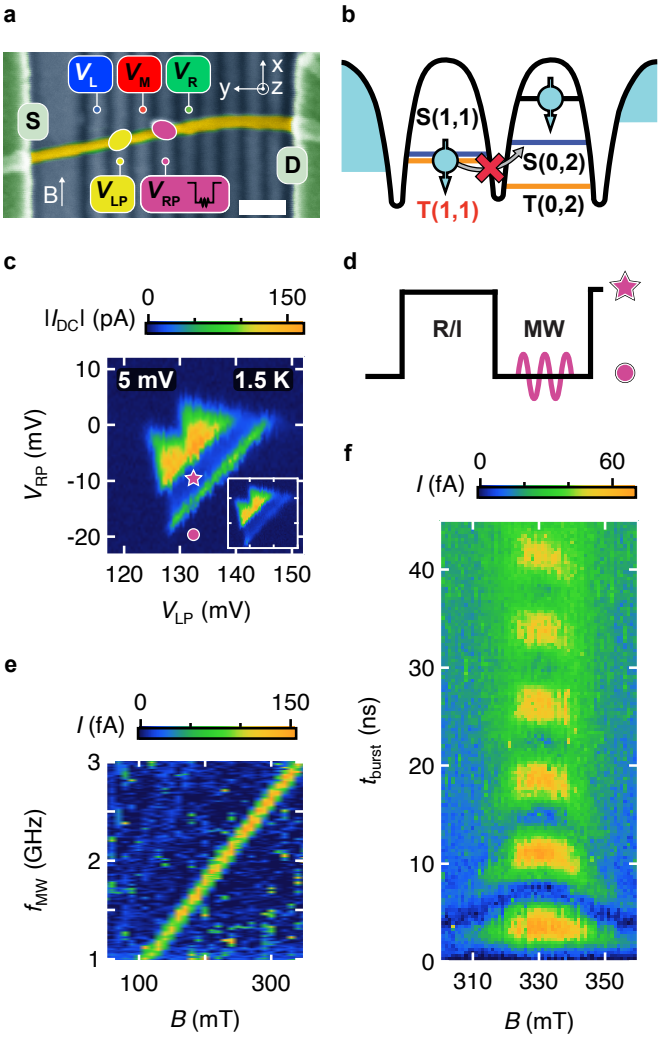

FIG. 1. **Measurement of a NW hole spin qubit at 1.5 K. a,** False-color scanning electron micrograph of a representative NW-device. The Ge/Si NW is highlighted in yellow, lying on top of nine bottom gates, and is further connected to source and drain contacts from above, marked S and D. The first five bottom gates from the left were used to form a DQD, whose expected location is indicated by the yellow and pink ovals. The colour code is consistently used throughout the manuscript. The scale bar corresponds to 100 nm. **b,** Schematic of PSB. In the absence of magnetic field and for detunings $\varepsilon < \varepsilon_{ST}$, charge transport is blocked when the system is initialised in a triplet state $T(1, 1)$. **c,** Measurement of bias triangles with lifted spin-blockade at $B = 350$ mT (x-direction) and bias of $V_{SD} = +5$ mV. The pink star marks the qubit initialisation/readout spot and the pink circle indicates the manipulation point. Inset: Same bias triangle at $B = 0$ mT, manifesting PSB via the suppressed current at the baseline. **d,** Schematic of the pulse scheme applied to V_{RP}, consisting of the readout/initialization stage (R/I) and the manipulation stage for which a MW burst is applied while in Coulomb blockade. **e,** Measurement of the current as a function of f_{MW} and **B** showing characteristic EDSR at a fixed microwave burst duration. **f,** Current as a function of microwave burst duration and magnetic field **B** at $f_L = 2.79$ GHz, showing Rabi-oscillations with a frequency $f_R = 130$ MHz and coherence time $T_2^{Rabi} = 40$ ns.

After a short waiting time, the system is pulsed into Coulomb blockade by applying a square voltage pulse, as indicated by the magenta circles in Figs. 1c and d. While in Coulomb blockade, a microwave (MW) burst of duration t_{burst} is applied. Pulsing back to the initial voltage of V_{RP} allows to record a current signal I, proportional to the likelihood of a singlet configuration after coherent manipulation. Fig. 1e shows typical EDSR measurements where the applied MW frequency f_{MW} is swept against the external magnetic field $\mathbf{B}$, and from which the g-factor is extracted. On resonance, the spin is rotated, lifting the spin-blockade which leads to an increased current. By varying the burst duration as a function of magnetic field detuning at a fixed frequency of the microwave drive f_{MW}, coherent Rabi oscillations can be observed as shown in Fig. 1f. These results establish coherent qubit control at 1.5 K.

To gather information about the level of control over the qubit, similar scans to those presented in Figs. 1e and f were repeated for different electrostatic environments experienced by the qubit whilst remaining within the same charge occupation of the DQD. Each electrostatic configuration of the qubit is defined by the three barrier gate voltages V_{L}, V_{M} and V_{R}, while the plunger gate voltages V_{LP} and V_{RP} were compensated to remain at a fixed readout point.

SOI in a Squeezed Quantum Dot

We characterize each qubit configuration by measuring the Rabi frequency f_{R} and Landé g-factor, g, and show their functional dependence on the three individual barrier voltages in Figs. 2a-c. In each of the three studies, the voltages on the other two barrier gates are held at a constant value, indicated by the vertical dashed lines in Figs. 2a-c. The larger responses of g and f_{R} to the barrier voltages V_{L} and V_{M}, compared to V_{R}, suggest that the qubit is located above the left plunger gate (LP). Moreover, the opposite trends of g and f_{R} with respect to voltage are consistent with the theoretical description of an elongated quantum dot in the presence of SOI [20]. To understand the observations made in Figs. 2a-c, we first explain how SOI renormalises the g-factor, followed by how it can be related to f_{R} by choosing a specific EDSR driving mechanism.

In the case of a quasi 1D, elongated quantum dot, as it is reasonable to assume for our NW, the longitudinal axis of gate-defined confinement is well described by a harmonic potential resulting in a Gaussian envelope of the hole wave function. In the presence of SOI, the spins acquire a helical texture along the NW [18–20, 41], provided the external magnetic field $\mathbf{B}$ acting on the g-tensor $\hat{\mathbf{g}}$ gives rise to a Zeeman vector $\hat{\mathbf{g}} \cdot \mathbf{B}$ with a component perpendicular to the SOI axis $\boldsymbol{\alpha}_{\mathrm{SO}}$. As a result, the hole wave function averages over different spin orientations, leading to a renormalization of the dot g-factor (see Eq. 1 I). This effect is especially relevant when the dot extension along the NW, l_{dot}, and spin-orbit length l_{SO}, which represents the distance a hole must traverse to undergo a spin rotation due to SOI, are comparable in size. This leads to a minimum in g-factor where the SOI is strongest, i.e. l_{SO} shortest. Relating g to f_{R}, however, additionally requires an assumption on the underlying qubit driving mechanism.

We assume that all effects arising from SOI, induced by a change in voltage ΔV, are captured by a modulation of the g-tensor [46] while keeping the magnetic field constant, that is $\hat{\mathbf{g}}_0 \cdot \mathbf{B} \xrightarrow{\Delta V} \hat{\mathbf{g}}_{\Delta V} \cdot \mathbf{B}$. We represent this as a rotation of the Zeeman vector around the perpendicular component of the spin-orbit vector, $\boldsymbol{\alpha}^{\perp}_{\mathrm{SO}}$. Periodic displacements of the wave function along the NW can result in SOI-mediated Rabi oscillations. We refer to them as iso-Zeeman EDSR (iso-EDSR), if they conserve the modulus of the Zeeman vector $|\hat{\mathbf{g}} \cdot \mathbf{B}|$, Fig. 2d left. In this case $f_{\mathrm{R}} \propto 1/l_{\mathrm{SO}}$ [42], and g can be directly related to f_{R} (see Eq. 1 II),

$$g \overset{\mathrm{I}}{=} g_{\mathrm{NW}} \cdot e^{-(l_{\mathrm{dot}}/l_{\mathrm{SO}})^2} \overset{\mathrm{II}}{=} g_{\mathrm{NW}} \cdot e^{-C \cdot f_{\mathrm{R}}^2} \quad . \tag{1}$$

Here, g denotes the measured g-factor as extracted from Fig. 1e, g_{NW} is an intrinsic NW g-factor without renormalization due to SOI, and C is a fitting parameter. The derivation is provided in the Supplementary Information. We further note that the functional form of Eq. 1 results from the harmonic confinement along the longitudinal axis of the NW and is independent of the microscopic origin of the SOI.

As seen in Eq. 1, when reducing l_{SO} (thereby increasing SOI), g is suppressed and f_{R} increased. This behaviour can be observed in Figs. 2a and b. To obtain a minimum in g and a maximum in f_{R}, as seen in Fig. 2a, the governing SOI has to plateau or show a maximum, as an implicit function of voltage. Ge/Si core-shell NWs as the one used here [7], like Ge-hut wires [37] and Si-FinFETs [16], particularly benefit from DRSOI which is expected to reach a local maximum at moderate electric fields below 10 MV/m [7, 18, 19, 39]. These predicted electric field ranges are consistent with the voltage range of $\sim$ 100 mV around the extrema of g and f_{R} shown in Fig. 2a, assuming a voltage drop over $\sim$ 50 nm (gate-pitch).

In order to facilitate iso-EDSR, displacements of the hole wave function along the NW are desirable, while only minimally varying the dot potential. To this end the MW drive is chosen at gate RP, located as far as possible from the qubit on gate LP. To see where the driving mechanism is consistent with iso-EDSR, we measure the response of g to variations ΔV_{RP}, to extract $\partial g/\partial V_{\mathrm{RP}}$ at a fixed magnetic field $\mathbf{B}$. These responses are shown in Figs. 2e and f, as a function of V_{L} and V_{M}.

If, while driving, the voltage shifts ΔV_{RP} cause significant variations of the target dot potential, the induced Rabi oscillations can be significantly influenced by g-tensor modulated EDSR (gtm-EDSR). Such modulations of the g-tensor do not conserve the modulus of the Zeeman vector $\hat{\mathbf{g}} \cdot \mathbf{B}$, Fig. 2d right. Since the response $\partial g/\partial V_{\mathrm{RP}}$ is computed from the difference in lengths of Zeeman vectors $|\hat{\mathbf{g}}_0 \cdot \mathbf{B}| - |\hat{\mathbf{g}}_{\Delta V_{\mathrm{RP}}} \cdot \mathbf{B}| = \Delta_{|\hat{\mathbf{g}} \cdot \mathbf{B}|}$ under ΔV_{RP}, we can only provide a rough upper bound to the g-tensor modulated Rabi contribution $f_{\mathrm{R}}^{\mathrm{gtm}}$ which is proportional to a transverse modulation of the Zeeman vector $\Delta^{\mathrm{gtm}}_{|\hat{\mathbf{g}} \cdot \mathbf{B}|}$. These approximate upper bounds for $f_{\mathrm{R}}^{\mathrm{gtm}} \propto |\Delta^{\mathrm{gtm}}_{|\hat{\mathbf{g}} \cdot \mathbf{B}|}/\Delta V_{\mathrm{RP}}| \leq |\Delta_{|\hat{\mathbf{g}} \cdot \mathbf{B}|}/\Delta V_{\mathrm{RP}}|$ are represented by the bars in Figs. 2a and b. For the calculation of $f_{\mathrm{R}}^{\mathrm{gtm}}$ and a qualitative description of the EDSR driving mechanisms we

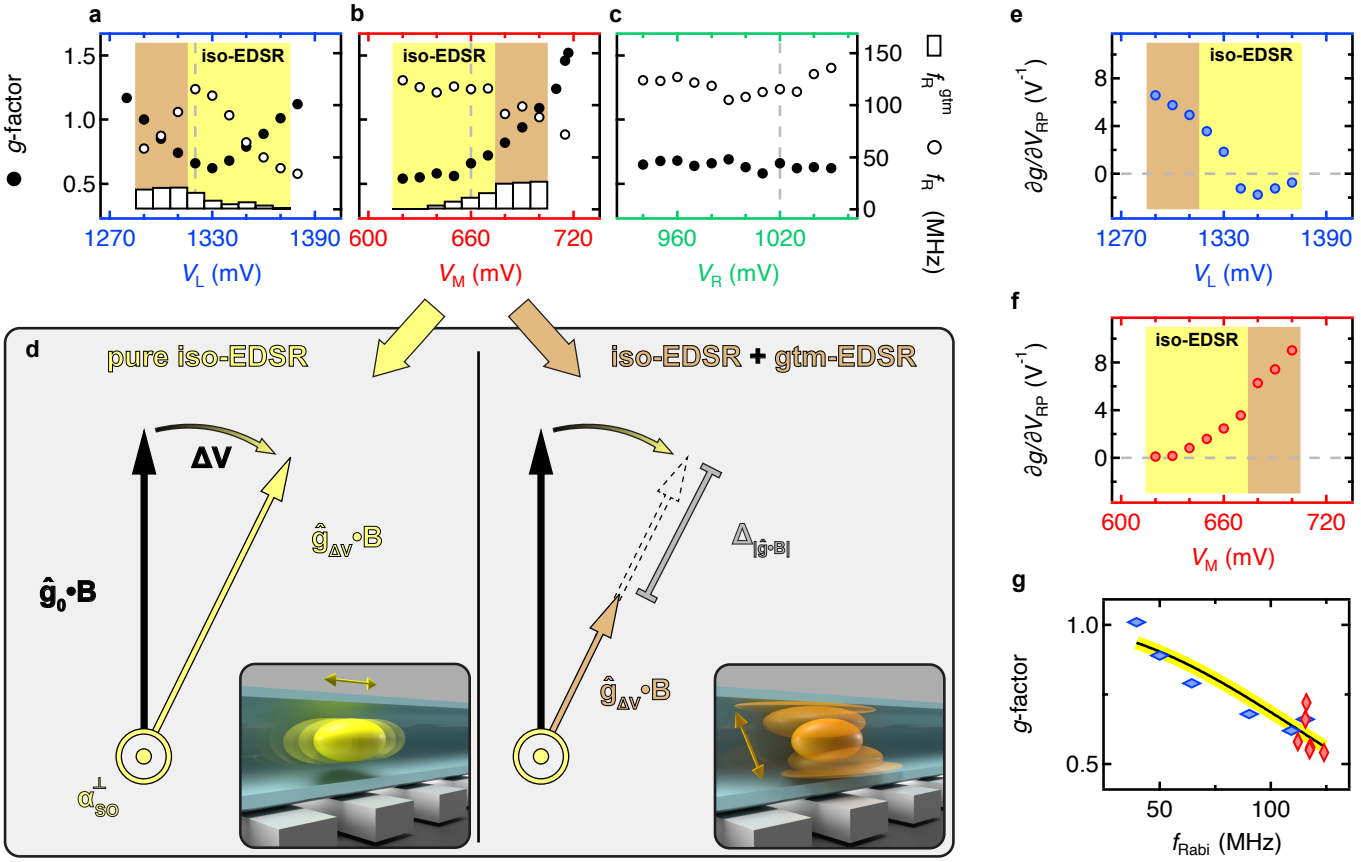

FIG. 2. **SOI mediated g-factor renormalization of an elongated dot. a-c,** Experimental data of the qubit g-factor (●), the corresponding Rabi frequency f_R (○) and the estimated gtm-EDSR contribution f_{gtm} (□), as a function of the barrier gate voltages V_L, V_M and V_R, respectively. For each of the datasets a-c, the values on the other two barrier gates are fixed at the value marked by the vertical dashed line. The yellow coloured regions highlight the voltage ranges for which the qubit driving mechanism is dominantly iso-EDSR, whereas the brown regions show the ranges for which the contribution to the measured f_R originating from gtm-EDSR, f_R^{gtm}, is ≥ 15% (5% above the spread of data points, see Supplementary Information). These colours are used consistently in all other panels. The estimated f_{gtm} is represented by the white bar charts. **d,** Schematic visualisation of how the Zeeman vector $\hat{\mathbf{g}}_0 \cdot \mathbf{B}$ is affected when subject to an infinitesimal voltage change dV in the presence of SOI represented by $\alpha_{SO}^{\perp}$ and a fixed magnetic field $|\mathbf{B}|$. Left shows pure iso-EDSR coming from displacements of the dot potential. Right shows the additional appearance of gtm-EDSR, when the dot is displaced and deformed. **e,** Shows the extracted $\partial g/\partial V_{RP}$, as a function of the voltage V_L in blue, and **f,** as a function of V_M in red. These derivatives are used to calculate an upper bound of the g-modulated contribution to f_R. **g,** g-factor as a function of f_R exclusively showing those data points for which iso-EDSR is the dominant driving mechanism, while the gtm-EDSR contribution is ≤ 15% of the measured f_R. We fit the data using Eq. 1 which assumes iso-EDSR (fit shown by black line with yellow highlight), yielding an intrinsic NW g-factor of $g_{NW} \approx 1$.

refer to the Supplementary Information.

As seen in Figs. 2a, b, e and f, we qualitatively divide the measured data points into two regions, driven primarily by pure iso-EDSR (yellow) and a mix of both, iso- and gtm-EDSR (brown). If $|\partial g/\partial V_{RP}| \to 0$, also the component attributed to gtm-EDSR, $f_R^{gtm} \to 0$. This leaves iso-EDSR as the only available mechanism that can induce Rabi oscillations.

The pairs of f_R and g classified as pure iso-EDSR are shown in Fig. 2g where they are fitted using Eq. 1. From the fit parameter $g_{NW} \approx 1$ and the experimental values of g, the corresponding l_{SO} were calculated yielding a range from 65 nm to 150 nm, assuming l_{dot} = 50 nm (gate pitch). It is worth noting that this estimation of l_{SO} does not rely on knowledge of the effective mass m_{eff}, which can be challenging to estimate in systems with HH-LH mixing, as the one studied here. Further, the calculated values of l_{SO} are in agreement with those obtained via magnetic field spectroscopy [41] and qubit measurements in Ref. [7] assuming HH-LH mixing.

Compromise-Free Operation

Given the extremal behaviour of the g-factor and f_R from Fig. 2a, we measured the Hahn-echo decay times T_2^{Hahn} as a function of V_L and compare them in Fig. 3a. We note that T_2^* was too short to be reliably extracted, due to its sensitivity to low-frequency noise and the long integration times required by our transport measurements.

The applied pulse sequence involved a $\pi_x/2$ pulse, a refocusing π pulse, and a $\pi_\varphi/2$ pulse with a sinusoidally varying phase as a function of the free evolution time τ, allowing

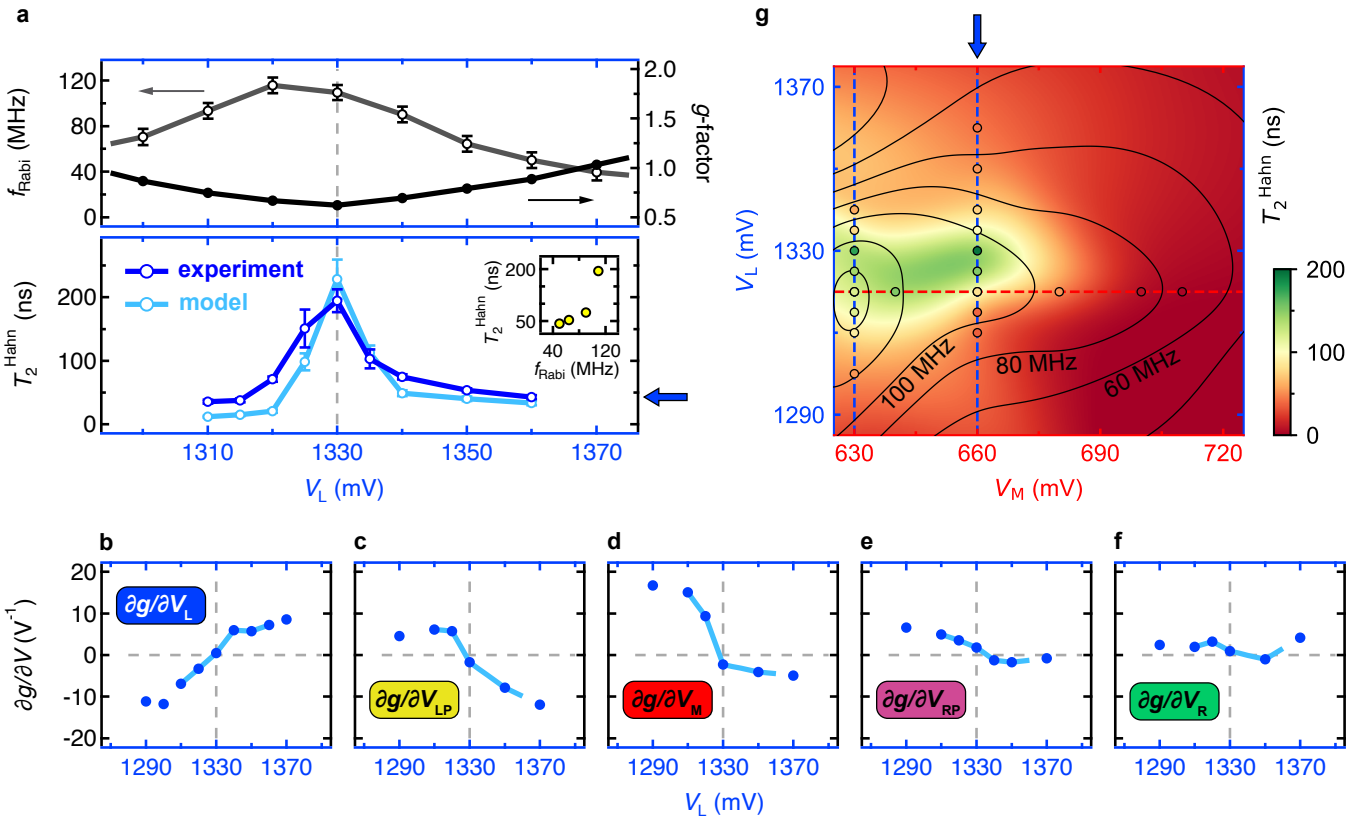

FIG. 3. **Compromise-free operation. a,** The top plot shows the experimental f_R and g as a function of V_L. The bottom plot shows the coherence times T_2^{Hahn} (dark blue) obtained from fits of the time-dependent readout current measured in Hahn-echo experiments at different gate voltages V_L. The light blue data shows the modelled coherence times taking into account $g_i'(V_L)$ from panels b-f using Eq. 2, yielding $S_G = 29$ nV/$\sqrt{\text{Hz}}$. The vertical dashed line at $V_L = 1330$ mV shows the sweet spot at which T_2^{Hahn} is maximal. This spot coincides with the fastest f_R within experimental errors. The inset shows pairs of f_R and g to the right of $V_L = 1330$ mV. **b-f,** Show $g_i'(V_L) := \partial g/\partial V_i(V_L)$, as a function of different static voltages on the left barrier gate V_L. The dark blue data points represent values of V_L for which the $g_i'(V_L)$ were measured. The light blue line corresponds to linearly interpolated data points in order to match the number of measured data points between $g_i'(V_L)$ and T_2^{Hahn}, which was fitted in panel a. The vertical dashed line marks the sweet spot at $V_L = 1330$ mV for which all five $g_i'(V_L)$ reach near zero, defining the sweet spot. The horizontal dashed line marks the zero-line of the $g_i'(V_L)$. **g,** The *FACTOR*: 2D voltage space showing T_2^{Hahn} as a function of gate voltages V_M and V_L. The filled circles represent the measured coherence times T_2^{Hahn} extracted analogously to panel a. The data trace corresponding to the dark blue trace on panel a is referenced by the blue arrow on the 2D plot. An additional trace of T_2^{Hahn} as a function of V_L for fixed $V_M = 630$ mV is indicated by the vertical dark blue dashed line on the left end of the plot, as well as a trace of T_2^{Hahn} as a function of V_M for fixed $V_L = 1320$ mV which is indicated by the horizontal red dashed line. The background is obtained by a Gaussian process interpolation and serves as a guide to the eye. The black contours show a Gaussian process interpolation of measured Rabi frequencies, to highlight the overlap of maxima in T_2^{Hahn} and f_R.

for a more robust fit of the Hahn decay. Assuming $1/f^\beta$ noise, the exponent of the Hahn-echo decay $\alpha = 1 + \beta$ was defined as a global fit parameter, shared among all data sets, and converged to $\alpha \approx 1$. This value for α was extracted for the frequency range sampled by the Hahn-echo experiment from approximately $1/\tau_{max} = 12.5$ MHz up to f_R. Given the operation temperature of 1.5 K, a white noise spectrum could be expected, as observed in other spin qubit experiments [16, 17, 47, 48]. Above 1.7 K, the qubit readout in this device significantly degrades. As seen in Fig. 3a, the coherence peaks at a gate voltage V_L where the g-factor is minimal and f_R is maximal. This observation clearly indicates a compromise-free scaling regime in which the fastest qubit operation times coincide with the coherence sweet spot. Further, the qualitative signature of the sweet spot remains robust regardless of the choice of noise color β, as shown in the Supplementary Information.

Next, we analyze the response of g to small voltage fluctuations of the gate voltages V_i as a function of V_L, denoted as $\partial g/\partial V_i(V_L)$. We refer to $\partial g/\partial V_i(V_L)$ as $g_i'(V_L)$ for brevity. Figs. 3b-f show the $g_i'(V_L)$ of the five gates used in our experiments. One striking commonality among all five $g_i'(V_L)$ is the near-zero point crossing at the sweet spot voltage $V_L^* = 1330$ mV, indicating minimal modulations of the Zeeman vector magnitude $|\hat{\mathbf{g}} \cdot \mathbf{B}|$.

We suspect the noise to mainly originate from charge traps in the self-terminated, native SiO_2 layer, which uniformly covers the $\sim$ 2 nm thick NW shell. This brings a source of noise very close to the Ge core, where the hole wave function resides. We model the noise as voltage fluctuations on all

the gates with one common noise spectrum, characterized by a spectral density S_G and exponent β. Considering the appropriate noise filter function for a Hahn-echo and $\beta = 0$ (as determined before), the characteristic decay rate can be expressed as [4],

$$\frac{1}{T_2^{\text{Hahn}}} = 2\pi^2 \left(\sum_i \left(\frac{\partial g}{\partial V_i} S_G \right)^2 \right) \quad . \tag{2}$$

The best fit to the measured T_2^{Hahn}, employing Eq. 2, is obtained with a white noise spectral density of $S_G(f_0/f) = 29\ \text{nV}/\sqrt{\text{Hz}}$, with $f_0 = 12.5$ MHz. The modeled coherence times are shown in Fig. 3a. No additional lever arms are required in Eq. 2, as they are already captured by the $g_i'(V_L)$. Lastly, we repeat similar coherence measurements for different values of V_M and show in Fig. 3g that the *FACTOR* is not limited to a point in voltage space. In fact, the existence of a "sweet ridge" can be observed, which shows a weaker dependence of the coherence time T_2^{Hahn} on V_M as compared to V_L, over comparable voltage ranges. As shown by the black contours in Fig. 3g, the Rabi frequency f_R follows the trend of T_2^{Hahn}, reaching frequencies above 100 MHz surrounding the coherent region in green. The experimental data points for the contour plot of f_R are shown in the Supplementary Information.

Conclusions

We report on the existence of a *FACTOR* for which the coherence sweet spot coincides with the fastest qubit operation speeds. We demonstrate that our *FACTOR* originates from the renormalisation of the g-factor yielding a minimum in g and thus $g_i'(V_L) = 0$, when the SOI is maximised for a hole quantum dot subject to strong, quasi 1D confinement. Further, maximal Rabi frequencies are achieved for iso-EDSR driving of the qubit. We favour this driving mechanism by applying the MW drive to a remote gate, and identify static gate voltage ranges for which the qubit is indeed dominantly driven by iso-EDSR. Our observations are in agreement with theoretical predictions for holes under quasi 1D confinement and a comparable Rashba-type SOI [20, 21]. Additionally, our *FACTOR* can be tuned all-electrically at the individual qubit level, without the need of changing global experimental parameters. Our experimental observations thus overturn the conventional wisdom that fast qubit operations impose a toll on qubit life times.

The conditions leading to the observed compromise-free operation might be translated to 2D hole spin qubit platforms using lateral squeezing gate electrodes to induce strong, quasi 1D confinement [20]. Regarding the applicability for electrons, conventional Rashba SOI could potentially also be tuned by electric fields to reach a maximum in SOI, but might require larger electric fields than the ones used here, as the SOI is primarily governed by the fundamental band gap of the semiconductor obtained in the third order of a multi-band perturbation theory [49, 50]. For systems using synthetic SOI generated by micro-magnets, strategic placement of the QD, relative to the magnet using static gates, might give rise to a voltage tunable maximum of the synthetic SOI experienced by the QD [51]. Finally, it is essential for the SOI to be strong enough to enter the strong SOI regime, for which $l_{SO} \approx l_{dot}$ holds.

Furthermore, we have established coherent control of a hole spin qubit in a Ge/Si NW at 1.5 K, with qubit operation speeds and coherence times on par with previous experiments performed at mK temperatures [7]. This achievement renders our platform compatible with on-chip classical control electronics [52].

By demonstrating the feasibility of a *FACTOR* in a hole spin qubit, our work offers a new angle from which to approach fault-tolerant quantum computation without sacrificing high qubit operation speeds.

[1] J. Yoneda, K. Takeda, T. Otsuka, T. Nakajima, M. R. Delbecq, G. Allison, T. Honda, T. Kodera, S. Oda, Y. Hoshi, N. Usami, K. M. Itoh, and S. Tarucha, Nature Nanotechnology **13**, 102 (2017).

[2] N. W. Hendrickx and A. Fuhrer, Nature Nanotechnology **17**, 1040 (2022).

[3] T. Tanttu, B. Hensen, K. W. Chan, C. H. Yang, W. W. Huang, M. Fogarty, F. Hudson, K. Itoh, D. Culcer, A. Laucht, A. Morello, and A. Dzurak, Physical Review X **9**, 021028 (2019).

[4] N. Piot, B. Brun, V. Schmitt, S. Zihlmann, V. P. Michal, A. Apra, J. C. Abadillo-Uriel, X. Jehl, B. Bertrand, H. Niebojewski, L. Hutin, M. Vinet, M. Urdampilleta, T. Meunier, Y.-M. Niquet, R. Maurand, and S. D. Franceschi, Nature Nanotechnology **17**, 1072 (2022).

[5] N. W. Hendrickx, L. Massai, M. Mergenthaler, F. Schupp, S. Paredes, S. W. Bedell, G. Salis, and A. Fuhrer, arXiv (2023), 10.48550/ARXIV.2305.13150.

[6] S. Bosco, B. Hetényi, and D. Loss, PRX Quantum **2**, 010348 (2021).

[7] F. N. M. Froning, L. C. Camenzind, O. A. H. van der Molen, A. Li, E. P. A. M. Bakkers, D. M. Zumbühl, and F. R. Braakman, Nature Nanotechnology **16**, 308 (2021).

[8] W. Gilbert, T. Tanttu, W. H. Lim, M. Feng, J. Y. Huang, J. D. Cifuentes, S. Serrano, P. Y. Mai, R. C. C. Leon, C. C. Escott, K. M. Itoh, N. V. Abrosimov, H.-J. Pohl, M. L. W. Thewalt, F. E. Hudson, A. Morello, A. Laucht, C. H. Yang, A. Saraiva, and A. S. Dzurak, Nature Nanotechnology **18**, 131 (2023).

[9] J. J. Pla, K. Y. Tan, J. P. Dehollain, W. H. Lim, J. J. L. Morton, F. A. Zwanenburg, D. N. Jamieson, A. S. Dzurak, and A. Morello, Nature **496**, 334 (2013).

[10] M. Veldhorst, C. H. Yang, J. C. C. Hwang, W. Huang, J. P. Dehollain, J. T. Muhonen, S. Simmons, A. Laucht, F. E. Hudson, K. M. Itoh, A. Morello, and A. S. Dzurak, Nature **526**, 410 (2015).

[11] N. W. Hendrickx, W. I. L. Lawrie, L. Petit, A. Sammak, G. Scappucci, and M. Veldhorst, Nature Communications **11** (2020), 10.1038/s41467-020-17211-7.

[12] N. W. Hendrickx, D. P. Franke, A. Sammak, G. Scappucci, and M. Veldhorst, Nature **577**, 487 (2020).

[13] H. Liu, K. Wang, F. Gao, J. Leng, Y. Liu, Y.-C. Zhou, G. Cao, T. Wang, J. Zhang, P. Huang, H.-O. Li, and G.-P. Guo, Nano Letters **23**, 3810 (2023).

[14] C. H. Yang, R. C. C. Leon, J. C. C. Hwang, A. Saraiva, T. Tanttu, W. Huang, J. Camirand Lemyre, K. W. Chan, K. Y. Tan, F. E. Hudson, K. M. Itoh, A. Morello, M. Pioro-Ladrière, A. Laucht, and A. S. Dzurak, Nature **580**, 350 (2020).

[15] L. Petit, H. G. J. Eenink, M. Russ, W. I. L. Lawrie, N. W. Hendrickx, S. G. J. Philips, J. S. Clarke, L. M. K. Vandersypen, and M. Veldhorst, Nature **580**, 355 (2020).

[16] L. C. Camenzind, S. Geyer, A. Fuhrer, R. J. Warburton, D. M. Zumbühl, and A. V. Kuhlmann, Nature Electronics **5**, 178 (2022).

[17] J. Y. Huang, R. Y. Su, W. H. Lim, M. Feng, B. van Straaten, B. Severin, W. Gilbert, N. D. Stuyck, T. Tanttu, S. Serrano, J. D. Cifuentes, I. Hansen, A. E. Seedhouse, E. Vahapoglu, N. V. Abrosimov, H.-J. Pohl, M. L. W. Thewalt, F. E. Hudson, C. C. Escott, N. Ares, S. D. Bartlett, A. Morello, A. Saraiva, A. Laucht, A. S. Dzurak, and C. H. Yang, arXiv (2023), 10.48550/ARXIV.2308.02111.

[18] C. Kloeffel, M. Trif, and D. Loss, Physical Review B **84**, 195314 (2011).

[19] C. Kloeffel, M. J. Rančić, and D. Loss, Physical Review B **97**, 235422 (2018).

[20] S. Bosco, M. Benito, C. Adelsberger, and D. Loss, Physical Review B **104**, 115425 (2021).

[21] Z. Wang, E. Marcellina, A. R. Hamilton, J. H. Cullen, S. Rogge, J. Salfi, and D. Culcer, npj Quantum Information **7** (2021), 10.1038/s41534-021-00386-2.

[22] V. P. Michal, J. C. Abadillo-Uriel, S. Zihlmann, R. Maurand, Y.-M. Niquet, and M. Filippone, Physical Review B **107**, l041303 (2023).

[23] C. Kloeffel, M. Trif, P. Stano, and D. Loss, Physical Review B **88**, 241405 (2013).

[24] S. Bosco, P. Scarlino, J. Klinovaja, and D. Loss, Physical Review Letters **129**, 066801 (2022).

[25] D. Loss and D. P. DiVincenzo, Physical Review A **57**, 120 (1998).

[26] P. Stano and D. Loss, Nature Reviews Physics **4**, 672 (2022).

[27] G. Burkard, T. D. Ladd, A. Pan, J. M. Nichol, and J. R. Petta, Reviews of Modern Physics **95**, 025003 (2023).

[28] A. Laucht, R. Kalra, S. Simmons, J. P. Dehollain, J. T. Muhonen, F. A. Mohiyaddin, S. Freer, F. E. Hudson, K. M. Itoh, D. N. Jamieson, J. C. McCallum, A. S. Dzurak, and A. Morello, Nature Nanotechnology **12**, 61 (2016).

[29] N. W. Hendrickx, W. I. L. Lawrie, M. Russ, F. van Riggelen, S. L. de Snoo, R. N. Schouten, A. Sammak, G. Scappucci, and M. Veldhorst, Nature **591**, 580 (2021).

[30] S. G. J. Philips, M. T. Madzik, S. V. Amitonov, S. L. de Snoo, M. Russ, N. Kalhor, C. Volk, W. I. L. Lawrie, D. Brousse, L. Tryputen, B. P. Wuetz, A. Sammak, M. Veldhorst, G. Scappucci, and L. M. K. Vandersypen, Nature **609**, 919 (2022).

[31] A. M. J. Zwerver, T. Krähenmann, T. F. Watson, L. Lampert, H. C. George, R. Pillarisetty, S. A. Bojarski, P. Amin, S. V. Amitonov, J. M. Boter, R. Caudillo, D. Correas-Serrano, J. P. Dehollain, G. Droulers, E. M. Henry, R. Kotlyar, M. Lodari, F. Lüthi, D. J. Michalak, B. K. Mueller, S. Neyens, J. Roberts, N. Samkharadze, G. Zheng, O. K. Zietz, G. Scappucci, M. Veldhorst, L. M. K. Vandersypen, and J. S. Clarke, Nature Electronics **5**, 184 (2022).

[32] S. Neyens, O. Zietz, T. Watson, F. Luthi, A. Nethwewala, H. George, E. Henry, A. Wagner, M. Islam, R. Pillarisetty, R. Kotlyar, K. Millard, S. Pellerano, N. Bishop, S. Bojarski, J. Roberts, and J. S. Clarke, "Probing single electrons across 300 mm spin qubit wafers," (2023).

[33] A. J. Weinstein, M. D. Reed, A. M. Jones, R. W. Andrews, D. Barnes, J. Z. Blumoff, L. E. Euliss, K. Eng, B. H. Fong, S. D. Ha, D. R. Hulbert, C. A. C. Jackson, M. Jura, T. E. Keating, J. Kerckhoff, A. A. Kiselev, J. Matten, G. Sabbir, A. Smith, J. Wright, M. T. Rakher, T. D. Ladd, and M. G. Borselli, Nature **615**, 817 (2023).

[34] G. Scappucci, C. Kloeffel, F. A. Zwanenburg, D. Loss, M. Myronov, J.-J. Zhang, S. De Franceschi, G. Katsaros, and M. Veldhorst, Nature Reviews Materials **6**, 926 (2020).

[35] Y. Fang, P. Philippopoulos, D. Culcer, W. A. Coish, and S. Chesi, Materials for Quantum Technology **3**, 012003 (2023).

[36] K. C. Nowack, F. H. L. Koppens, Y. V. Nazarov, and L. M. K. Vandersypen, Science **318**, 1430 (2007).

[37] H. Watzinger, J. Kukučka, L. Vukušić, F. Gao, T. Wang, F. Schäffler, J.-J. Zhang, and G. Katsaros, Nature Communications **9** (2018), 10.1038/s41467-018-06418-4.

[38] L. Massai, B. Hetényi, M. Mergenthaler, F. J. Schupp, L. Sommer, S. Paredes, S. W. Bedell, P. Harvey-Collard, G. Salis, A. Fuhrer, and N. W. Hendrickx, arXiv (2023), 10.48550/ARXIV.2310.05902, arXiv:2310.05902 [cond-mat.mes-hall].

[39] C. Adelsberger, M. Benito, S. Bosco, J. Klinovaja, and D. Loss, Physical Review B **105**, 075308 (2022).

[40] L. Mauro, E. A. Rodríguez-Mena, M. Bassi, V. Schmitt, and Y.-M. Niquet, arXiv (2023), 10.48550/ARXIV.2312.09840, arXiv:2312.09840 [cond-mat.mes-hall].

[41] F. N. M. Froning, M. J. Rančić, B. Hetényi, S. Bosco, M. K. Rehmann, A. Li, E. P. A. M. Bakkers, F. A. Zwanenburg, D. Loss, D. M. Zumbühl, and F. R. Braakman, Physical Review Research **3**, 013081 (2021).

[42] V. N. Golovach, M. Borhani, and D. Loss, Physical Review B **74**, 165319 (2006).

[43] F. N. M. Froning, M. K. Rehmann, J. Ridderbos, M. Brauns, F. A. Zwanenburg, A. Li, E. P. A. M. Bakkers, D. M. Zumbühl, and F. R. Braakman, Applied Physics Letters **113** (2018), 10.1063/1.5042501.

[44] J. H. Ungerer, P. Chevalier Kwon, T. Patlatiuk, J. Ridderbos, A. Kononov, D. Sarmah, E. P. A. M. Bakkers, D. Zumbühl, and C. Schönenberger, Materials for Quantum Technology **3**, 031001 (2023).

[45] R. Maurand, X. Jehl, D. Kotekar-Patil, A. Corna, H. Bohuslavskyi, R. Laviéville, L. Hutin, S. Barraud, M. Vinet, M. Sanquer, and S. D. Franceschi, Nature Communications **7** (2016), 10.1038/ncomms13575.

[46] A. Crippa, R. Maurand, L. Bourdet, D. Kotekar-Patil, A. Amisse, X. Jehl, M. Sanquer, R. Laviéville, H. Bohuslavskyi, L. Hutin, S. Barraud, M. Vinet, Y.-M. Niquet, and S. D. Franceschi, Physical Review Letters **120**, 137702 (2018).

[47] L. Petit, J. Boter, H. Eenink, G. Droulers, M. Tagliaferri, R. Li, D. Franke, K. Singh, J. Clarke, R. Schouten, V. Dobrovitski, L. Vandersypen, and M. Veldhorst, Physical Review Letters **121**, 076801 (2018).

[48] S. D. Liles, D. J. Halverson, Z. Wang, A. Shamim, R. S. Eggli, I. K. Jin, J. Hillier, K. Kumar, I. Vorreiter, M. Rendell, J. H. Huang, C. C. Escott, F. E. Hudson, W. H. Lim, D. Culcer, A. S. Dzurak, and A. R. Hamilton, arXiv (2023), 10.48550/ARXIV.2310.09722.

[49] R. Winkler, "Spin-orbit coupling effects in two-dimensional electron and hole systems," (2003).

[50] M. J. Carballido, C. Kloeffel, D. M. Zumbühl, and D. Loss, Physical Review B **103**, 195444 (2021).

[51] M. Aldeghi, R. Allenspach, and G. Salis, Applied Physics Letters **122** (2023), 10.1063/5.0139670.

[52] L. M. K. Vandersypen, H. Bluhm, J. S. Clarke, A. S. Dzurak, R. Ishihara, A. Morello, D. J. Reilly, L. R. Schreiber, and M. Veldhorst, npj Quantum Information **3** (2017), 10.1038/s41534-017-0038-y.

Methods

Device Fabrication. The QD device featured a set of nine bottom gates, each with a width of ∼ 20 nm and a pitch of ∼ 50 nm. The gates were fabricated on an intrinsic Si (100) chip with 290 nm of thermal SiO_2 using electron beam lithography (EBL). After cold development, the bottom gates were metallized with 1 nm/9 nm of Ti/Pd, respectively. To provide electrical insulation between the bottom gates and the NW, 175 cycles (∼ 200 nm) of Al_2O_3 were grown by atomic layer deposition at approximately 225° C using atomic layer deposition. In an effort to improve the quality of the gate dielectric, the chip underwent annealing in a 20 mbar forming gas atmosphere (N_2 92%, H_2 8%) for 15 minutes at 300° C, prior to NW deposition. Details on the impact of the annealing process on gate hysteresis and qubit coherence are described in the Supplementary Information.

A single Ge/Si core/shell NW was deterministically placed in a perpendicular orientation to the nine bottom gates. The NW has a core radius of ∼ 10 nm and a shell thickness of ∼ 2.5 nm. The exact in-plane angle, however, remains unknown. Subsequently, ohmic contacts were patterned by EBL and metallized with Ti/Pd layers of 0.3 nm/50 nm of Ti/Pd, respectively, following a 10 second dip in buffered hydrofluoric acid to locally remove the native SiO_2 layer in the defined contact region. Fig. 1a presents a scanning electron micrograph of an analogously fabricated device from the same batch, representative of the measured device.

Measurement Apparatus. The experimental setup featured a variable temperature insert (VTI) in a liquid helium bath with the sample mounted below the 1K pot (base temperature 1.5 K). The VTI was equipped with a solenoid magnet controlled by an Oxford Instruments IPS magnet power supply. DC voltages were supplied by a Basel Precision Instruments digital-to-analog converter (LNHR 927) and filtered on a dedicated filter PCB (second-order RC low-pass filter, cutoff frequency 8 kHz). Fast gate pulses and IQ control pulses were generated on a Tektronix AWG 5204. A Rohde & Schwarz SGS100A Vector Signal Generator was used to generate the qubit control pulses through IQ modulation. The gate- and control pulses were combined using a Wainwright WDKX11 diplexer and delivered to the sample PCB using attenuated coaxial lines. A bias-tee on the sample PCB was used to combine the high frequency pulses with a DC bias. The DC current through the NW was amplified by a Basel Precision Instruments current-to-voltage converter (LSK389A) with a gain of 10^9 and measured using a National Instruments DAQ card (USB-6363). The Vector Signal Generator output was pulse-modulated by a Zurich Instruments MFLI lock-in amplifier at 77.777 Hz to enhance the signal-to-noise ratio of the qubit measurements.

Data Analysis. The g-factors were measured as described in Fig. 1e, and were extracted for each considered electrostatic configuration defined by the barrier voltages V_L, V_M and V_R. The positions of the resonance condition, with respect to f_{MW} at fixed $\mathbf{B}$, are obtained by fitting each column to a Gaussian. The slope of a linear fit to the center positions of the Gaussians then yields the g-factor. The Rabi frequencies f_R were extracted from fits to $I(t) = I_{offset} + I_0 \sin(2\pi f_R t_{burst} + \phi_0)\exp(-t_{burst}/T_2^{Rabi})$. Here, I_{offset} is an offset, I_0 the amplitude, ϕ_0 a phase shift and T_2^{Rabi} the characteristic decay time. The characteristic decay times of each individual Hahn-echo experiment T_2^{Hahn} were obtained from a global fit of all echo-experiments using $I(t) = I_{offset} + I_0 \sin(2\pi f_\varphi \tau_{wait} + \phi_0)\exp(-(\tau/T_2^{Hahn})^\alpha)$, and one shared parameter $\alpha = \beta + 1$. Furthermore f_φ describes the frequency at which the phase of the pulse $\pi_\varphi/2$ was artificially varied as a function of the free evolution time τ.

Measurement Details. The derivatives $\partial g/\partial V_i(V_j) := g_i'(V_j)$ presented in Fig. 3b-f were extracted in three different ways at fixed f_{MW}: **i) $g_i'(\boldsymbol{V_L})$, for $i \in$ {LP, M, R} :** The readout point was defined by fixing all gate voltages. The derivatives were then obtained by recording the g-factors at manually varied voltages $\Delta V_i = 2 - 4$ mV, without loosing readout. **ii) $g_{RP}'(V_j)$, for $j \in$ {L, M}:** For a fixed readout point, the depth ΔV_{CP}, by which the system was pulsed into Coulomb blockade, was varied by up to 10 mV while all other voltages were held constant. Only the DC voltage on V_{RP} was algorithmically adjusted for each ΔV_{CP} by a linear correction factor in order to keep the readout point fixed. As in i), the derivatives were computed by fitting the slope of the recorded g-factor versus the variation of ΔV_{CP}. **iii) $g_L'(V_L)$:** We first computed the derivative of the recorded $g(V_L)$ presented in Fig. 2a with respect to V_L, yielding $g_L'(\tilde{V}_L)$. Here, $\tilde{V}_L$ is used to highlight that for each value of V_L, the voltage V_{LP} was compensated as otherwise the readout point would have been lost over the considered range of V_L due to the large cross-capacitance. Therefore, in order to obtain the true derivative $g_L'(V_L)$, the influence of V_{LP} was subtracted to first order via $g_L'(V_L) = g_L'(\tilde{V}_L) - g_{LP}'(V_L) \cdot \Delta V_{LP}/\Delta V_L$. Here, $g_{LP}'(V_L)$ is taken from i) and the compensation $\Delta V_{LP}/\Delta V_L \approx -0.49$.

All qubit measurements were performed at a microwave frequency of 2.79 GHz at $P_{MW} = -13.4$ dBm power and $V_{IQ} = 300$ mV amplitude IQ voltage, corresponding to an AC excitation of $V_{ac} = 7.8$ mV at the driving gate RP. The Rabi chevron shown in Fig. 1f was taken near the optimal operating regime at $V_L = 1320$ mV, $V_M = 660$ mV, $V_R = 1020$ mV. The EDSR resonance shown in Fig. 1e was recorded at a fixed $t_{burst} = 4$ ns.

The Hahn-echo experiments were taken at 2 seconds integration time and depending on amplitude of the transport current, up to 50 averages were taken of each trace to improve the signal to noise ratio.

Data Availability

The data supporting the plots of this paper are available at the Zenodo repository at https://doi.org/10.5281/zenodo.10223162?preview=1.

Acknowledgments

We thank Y.-M. Niquet, S. Geyer and F.N.M. Froning for the fruitful discussions. This work was supported by the NCCR SPIN, the Swiss Nanoscience Institute (SNI), the Georg H. Endress Foundation, the Swiss National Science Foundation (SNSF), the EU H2020 European Microkelvin Platform (EMP) project (Grant No. 824109) and the Topologically Protected and Scalable Quantum Bits (TOP-SQUAD) project (Grant No. 862046). L.C.C. acknowledges support from a Swiss NSF mobility fellowship (P2BSP2−200127).

Author Contributions

M.J.C., S.S., T.P. and D.M.Z. conceived of the project and planned the experiments. M.J.C., S.S. and P.C.K. fabricated the device. A.L. and E.P.A.M.B. synthesized the NWs. S.B. developed the theoretical framework for squeezed quantum dots with inputs from D.L.. R.M.K. studied the gate dielectric quality. M.J.C. and T.P. designed the experimental setup with inputs from L.C.C.. M.J.C., S.S. and T.P. executed the experiments. J.S. contributed to the extended data sets supervised by N.A.. M.J.C., R.S.E., T.P. and S.B. developed the requirements for a *FACTOR* and analyzed the data with input from J.C.E. and D.M.Z.. D.M.Z. supervised the project. M.J.C. wrote the manuscript with inputs from all the authors.

Supplementary Information: A Qubit with Simultaneously Maximized Speed and Coherence

Miguel J. Carballido,[1,*] Simon Svab,[1] Rafael S. Eggli,[1] Taras Patlatiuk,[1] Pierre Chevalier Kwon,[1] Jonas Schuff,[2] Rahel M. Kaiser,[1] Leon C. Camenzind,[1,†] Ang Li,[3,‡] Natalia Ares,[4] Erik P.A.M Bakkers,[3] Stefano Bosco,[1,§] J. Carlos Egues,[1,5] Daniel Loss,[1,6] and Dominik M. Zumbühl[1,¶]

[1]*Department of Physics, University of Basel, Klingelbergstrasse 82, CH-4056 Basel, Switzerland*
[2]*Department of Materials, University of Oxford, Oxford OX1 3PH, United Kingdom*
[3]*Department of Applied Physics, TU Eindhoven, Den Dolech 2, 5612 AZ Eindhoven, The Netherlands*
[4]*Department of Engineering Science, University of Oxford, Oxford OX1 3PJ, United Kingdom*
[5]*Instituto de Física de São Carlos, Universidade de São Paulo, 13560-970 São Carlos, São Paulo, Brazil*
[6]*CEMS, RIKEN, Wako, Saitama 351-0198, Japan*

(Dated: February 13, 2024)

CONTENTS

* miguel.carballido@unibas.ch
† Currently at: CEMS, RIKEN, Wako, Saitama 351-0198, Japan
‡ Currently at: Institute of Microstructure and Properties of Advanced materials, Beijing University of Technology, Beijing, 100124, China
§ Currently at: QuTech and Kavli Institute of Nanoscience, Delft University of Technology, Delft, The Netherlands
¶ dominik.zumbuhl@unibas.ch

S1. g-FACTOR RENORMALIZATION DUE TO SOI UNDER ISO-ZEEMAN DRIVING

Assuming a harmonic confinement potential along the longitudinal axis of the NW, and in the presence of SOI, the measured g-factor is renormalized by a Gaussian envelope function [1, 2],

$$g = g_{\mathrm{NW}} \ \exp - \left(\frac{l_{\mathrm{dot}}}{l_{\mathrm{SO}}}\right)^2 \qquad , \tag{1}$$

where g_{NW} is the intrinsic g-factor derived from the microscopic confinement of the NW, l_{dot} is the dot size along the direction of lowest confinement and l_{SO} is the spin-orbit length defined here as the distance a hole has to traverse along the NW to have its spin flipped due to SOI.

The application of an oscillating electric field to gate RP in the presence of SOI, gives rise to an oscillating effective magnetic field $B_{\mathrm{eff}}(t)$, with magnitude [3],

$$B_{\mathrm{eff}}(t) = 2B \ \frac{l_{\mathrm{dot}}^2}{l_{\mathrm{SO}}} \ \frac{eE_{\mathrm{MW}}(t)}{\Delta_{\mathrm{orb}}} \qquad , \tag{2}$$

where e is the elementary charge, E_{MW} is the a.c. electric field in the dot generated by the microwaves, $\Delta_{\mathrm{orb}} = \hbar^2 l_{\mathrm{dot}}^{-2} m_{\mathrm{eff}}^{-1}$ is the orbital level splitting with m_{eff} the effective hole mass. The effective magnetic field $\mathbf{B}_{\mathrm{eff}}(t)$, drives the Rabi oscillations, at the Rabi frequency $f_{\mathrm{R}} = g \ \mu_{\mathrm{B}} |\mathbf{B}_{\mathrm{eff}}|/2h$, with g parallel to $\mathbf{B}$ and h Planck's constant.

To stay on resonance, the variation of g, induced by changes of the electrostatic environment, is compensated with a proportional change of $\mathbf{B}$, to match the Larmor frequency set by a fixed MW frequency $hf_{\mathrm{MW}} = g\mu_{\mathrm{B}}|\mathbf{B}|$. This effectively makes f_{R} independent of g,

$$f_{\mathrm{R}} = \frac{f_{\mathrm{L}}}{l_{\mathrm{SO}}} \ \frac{l_{\mathrm{dot}}^2 \ e|E_{\mathrm{MW}}(t)|}{\Delta_{\mathrm{orb}}} \qquad . \tag{3}$$

Combining Eqs. 1 and 3, yields the relation between g and f_{R},

$$g = g_{\mathrm{NW}} \ \exp - \left(C \cdot f_{\mathrm{R}}^2\right) \qquad , \tag{4}$$

with the fitting constant $C = \Delta_{\mathrm{orb}}^3 \ m_{\mathrm{eff}} \ f_{\mathrm{MW}}^{-2} \ \hbar^{-2} \ e^{-2} \ |E_{\mathrm{MW}}|^{-2}$. Fig. S1 shows the estimated orbital spacings Δ_{orb} as a function of V_{L} and V_{M} to be roughly constant over the operated voltage range. Here $|E_{\mathrm{MW}}|$ is constant as the frequency and power of the microwave signal were held constant for all experiments.

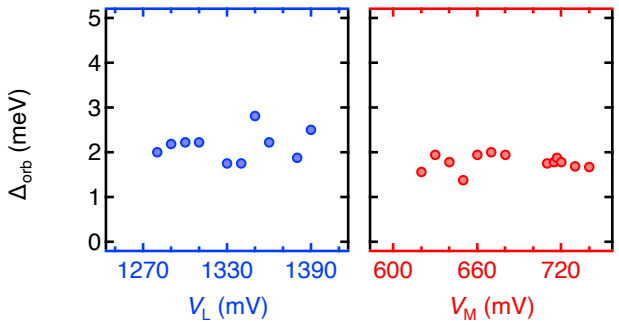

FIG. S1. **Estimation of Δ_{orb}.** Extracted from the ratio between the separation from the bias triangle base line to the first excited state, divided by the triangle height at $V_{SD} = 5$ mV, as a function of V_L (left) and V_M (right).

S2. EXPERIMENTAL ERROR ON f_R

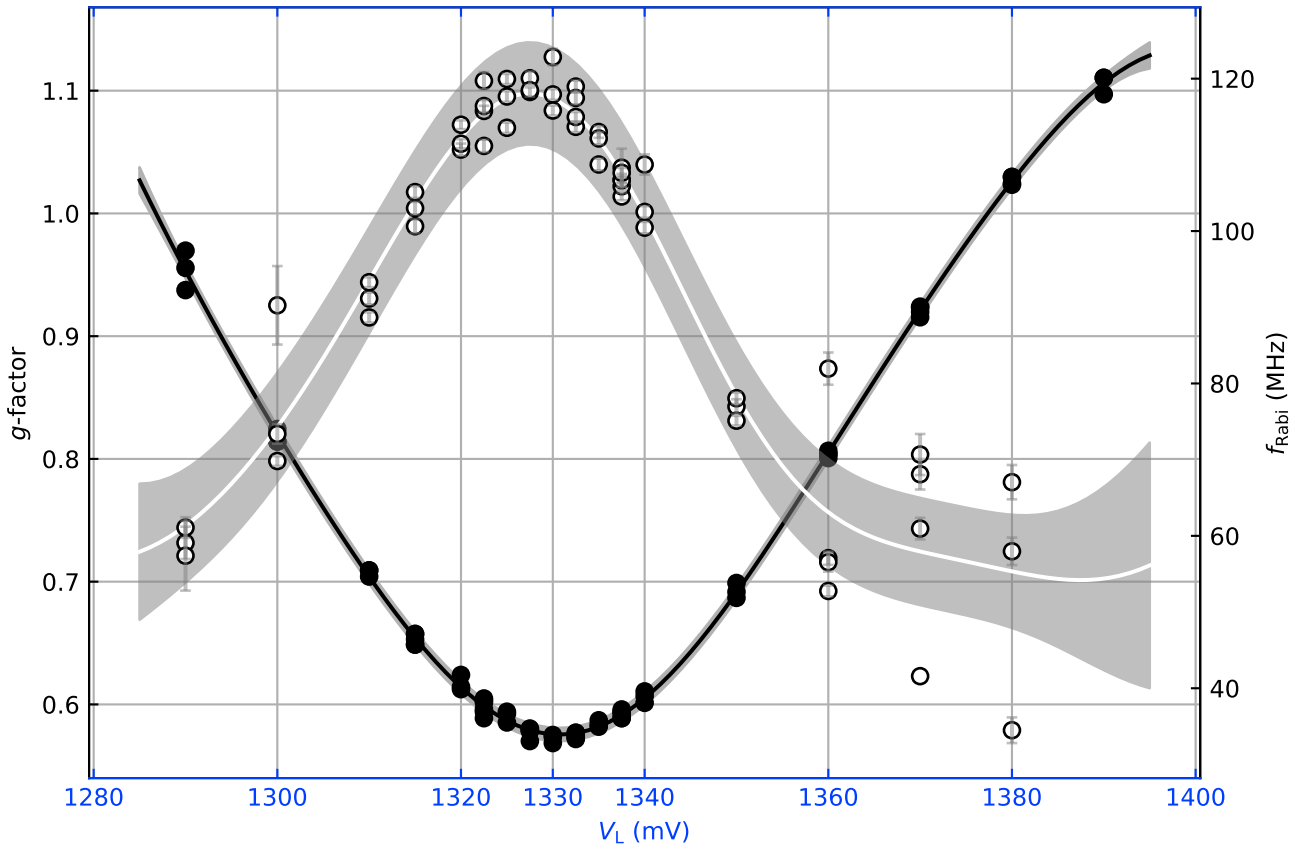

FIG. S2. **Reproducibility of the extrema in f_R and g.** Experimental data of the qubit g-factor (●) and Rabi frequency f_{Rabi} (○), as a function of the left barrier gate voltage V_L, at fixed gate voltages V_M = 660 mV and V_R = 1020 mV. The fit uncertainty of the measured Rabi oscillations is illustrated by grey error bars. For both the g-factor and f_R, Gaussian process fits are applied using a radial basis function kernel. The solid lines denote the average prediction of the Gaussian processes, while the shaded bands show the uncertainty of the Gaussian processes corresponding to one standard deviation.

The data series presented in Fig. S2 was collected in multiple sequences from low to high V_L. The extremal points of f_R and g coincide within 5 mV considering the experimental variation between runs. For f_R this variation corresponds to ~ 10 MHz around the maximum, while the variation of the g is negligibly small.

The observed spread of the measured quantities between runs can be attributed to slight variations of the readout point, in turn slightly varying g and f_R. Furthermore, charge switchers which shift the readout point relative to the bias triangle can influence g and f_R as well. We note that the traces presented in Fig. S2 were taken at a far later point in time relative to the first measured data points which were presented in the main section. Additionally the sample has experienced several thermal cycles from 1.5 K to 9 K. Taking into account both these circumstances and the reproducibility of the data, speaks for the stability of the device and the observed effects. To more accurately explain differences in the extremal points of f_R and g with regards to their positioning in gate voltage V_L, a more detailed model must be considered which captures voltage dependences of the intrinsic NW g-factor g_0, which in this work was assumed to be constant.

S3. POSSIBLE MANIFESTATIONS OF G-TENSOR MODULATION VS ISO-ZEEMAN DRIVING ON THE MEASURED ZEEMAN VECTOR

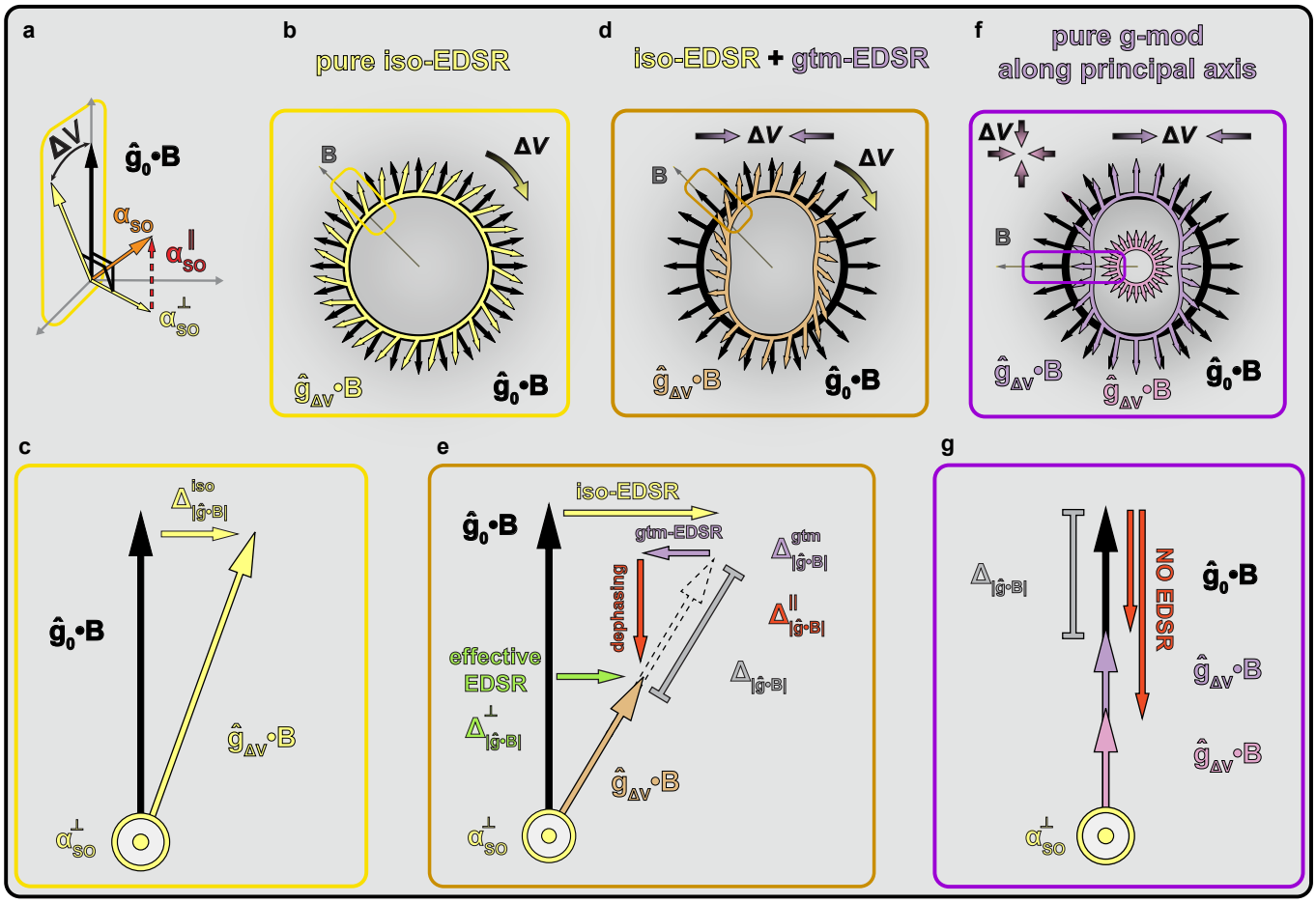

FIG. S3. **Possible manifestations of qubit driving mechanisms on the measured Zeeman vector. a,** Decomposition of the effective spin-orbit vector $\boldsymbol{\alpha}_{\mathrm{SO}}$, into perpendicular $\boldsymbol{\alpha}^{\perp}_{\mathrm{SO}}$ and parallel $\boldsymbol{\alpha}^{\parallel}_{\mathrm{SO}}$ components relative to $\hat{\mathbf{g}}_0 \cdot \mathbf{B}$. **b,** Shown in black is the Zeeman vector field of an arbitrary, here isotropic, g-tensor $\hat{g}_0$. Each vector represents a specific direction of magnetic field $\mathbf{B}$ with constant magnitude. Yellow shows the Zeeman vector field in the case of iso-EDSR, for which the magnitude of an arbitrary Zeeman vector is conserved, and the vector is solely rotated proportional to the strength of SOI and applied amplitude ΔV. No distortions of the g-tensor and therefore Zeeman vector field are present. **c,** Blown up image of one specific direction of B as indicated in grey in panel b. To first order, the only component acting on the incident Zeeman vector is perpendicular (small angle between $\hat{\mathbf{g}}_0 \cdot \mathbf{B}$ and $\hat{\mathbf{g}}_{\Delta V} \cdot \mathbf{B}$. **d,** Zeeman vector field showing the manifestation of both, iso-EDSR and gtm-EDSR (brown). **e,** The length of the Zeeman vector is not conserved. The perpendicular component to the drive originating from modulations of the g-tensor (violet), in this specific example, counteracts the pure iso-EDSR drive (yellow) resulting in an effective EDSR which induces the Rabi oscillations (green). **f-g,** Edge cases when the g-tensor modulations occur along the principal magnetic axes (purple) or the dot is symmetrically compressed (or expanded) in the form of a "breathing"-mode (pink), which do not give rise to EDSR.

Provided a constant magnetic field $\mathbf{B}$, we capture all effects arising from SOI induced by periodic voltage displacements ΔV, by changes of the g-tensor [4]. Formally, that is $\hat{\mathbf{g}}_0 \cdot \mathbf{B} \xrightarrow{\Delta V} \hat{\mathbf{g}}_{\Delta V} \cdot \mathbf{B}$. Further, we consider solely the vectorial component of the effective spin-orbit vector $\boldsymbol{\alpha}_{\mathrm{SO}}$ that is perpendicular to $\hat{\mathbf{g}}_0 \cdot \mathbf{B}$, hence $\boldsymbol{\alpha}^{\perp}_{\mathrm{SO}}$. Mechanisms involving the parallel component of $\boldsymbol{\alpha}_{\mathrm{SO}}$ with respect to $\hat{\mathbf{g}}_0 \cdot \mathbf{B}$, namely $\boldsymbol{\alpha}^{\parallel}_{\mathrm{SO}}$, and are responsible for e.g. the longitudinal driving of the spin through the application of an off-resonant microwave tone [5, 6], are not considered here. A vectorial decomposition of $\boldsymbol{\alpha}_{\mathrm{SO}}$ is shown in Fig. S3a.

In the case of SOI mediated Rabi oscillations, we can make a distinction between two EDSR driving mechanisms, based on the way they manifest on the magnitude of the resonant Zeeman vector. When the dot is subject to an infinitesimal change in voltage ΔV in the presence of SOI, the action of the induced effective magnetic field $\mathbf{B}_{\mathrm{SO}}$ around which the spin precesses, can

be represented by a rotation of the Zeeman vector $\hat{\mathbf{g}}_0 \cdot \mathbf{B}$ around $\boldsymbol{\alpha}_{\mathrm{SO}}^{\perp}$.

Assuming no further anisotropies of the g-tensor are introduced by ΔV, we define the induced rotations of the spin that arise while the modulus of the Zeeman vector is conserved, as iso-Zeeman EDSR (iso-EDSR), Fig. S3b. To first order, for a small enough variation ΔV, and thus small angle between $\hat{\mathbf{g}}_0 \cdot \mathbf{B}$ and $\hat{\mathbf{g}}_{\boldsymbol{\Delta V}} \cdot \mathbf{B}$, the only component acting on the incident Zeeman vector $\hat{\mathbf{g}}_0 \cdot \mathbf{B}$ is perpendicular, $\Delta^{\mathrm{iso}}_{|\hat{\mathbf{g}}\cdot\mathbf{B}|}$, Figs. S3c. As outlined in [3], iso-EDSR is expected to be the dominant qubit driving mechanism, whenever the motion of the dot induced by periodic voltage shifts ΔV does not come along significant variations of the dot potential.

Next, we classify contributions to EDSR that do not conserve the modulus of $\hat{\mathbf{g}}_0 \cdot \mathbf{B}$ as g-tensor modulated EDSR (gtm-EDSR). It arises whenever changes in the dot potential modulate the magnetic axes of the g-tensor and as a result anisotropically modify the Zeeman vector field, Fig. S3d. This mechanism introduces both, perpendicular $\Delta^{\mathrm{gtm}}_{|\hat{\mathbf{g}}\cdot\mathbf{B}|}$ and parallel $\Delta^{\parallel}_{|\hat{\mathbf{g}}\cdot\mathbf{B}|}$ components to the incident Zeeman vector, Fig. S3e. Usually, iso-EDSR is accompanied by gtm-EDSR, due to the fact that voltage changes on the gates which displace the dot likely also affect the potential landscape. In such cases, gtm-EDSR can counter act (or enhance) the driving component expected from pure iso-EDSR, yielding an effective EDSR drive $\Delta^{\perp}_{|\hat{\mathbf{g}}\cdot\mathbf{B}|} = \Delta^{\mathrm{iso}}_{|\hat{\mathbf{g}}\cdot\mathbf{B}|} \pm \Delta^{\mathrm{gtm}}_{|\hat{\mathbf{g}}\cdot\mathbf{B}|}$. It is not directly possible to derive the driving strength caused by gtm-EDSR from only measuring $\Delta_{|\hat{\mathbf{g}}\cdot\mathbf{B}|}$, as it is the case in our experiments. However, this absolute change in magnitude of the Zeeman vector does provide an upper bound on the g-tensor modulated contribution to the Rabi oscillations, $f_{\mathrm{R}}^{\mathrm{gtm}} \propto \Delta^{\mathrm{gtm}}_{|\hat{\mathbf{g}}\cdot\mathbf{B}|}$.

Finally, there remain some corner cases of highly symmetric modulations of the dot potential ("breathing modes"), or specific orientations of $\mathbf{B}$ which affect solely the principal magnetic axis longitudinally, and can be considered as pure g-tensor modulation, Fig. S3f. These scenarios however do not lead to Rabi oscillations, as they lack components perpendicular to the incident Zeeman vector and therefore do not induce EDSR, Fig. S3g.

S4. IMPACT OF THE GATE DIELECTRIC QUALITY ON QUBIT COHERENCE

Couplings to charge noise originating from impure oxides close to the quantum dot, in which the spin qubit is embedded, pose a limit for coherence [7, 8]. For the Ge/Si NW devices discussed in this work, the closest suspects are the native Silicon oxide on the shell of the nanowire and the ALD-grown Al_2O_3 oxide used as gate dielectric. Here, we investigate the impact of ALD-grown gate dielectric quality on the qubit coherence of our devices.

It has been reported that annealing of oxides can remove trapped charges at the oxide-semiconductor interface [9]. We thus compare whether an annealed ALD-grown oxide layer shows any improvement of qubit coherence times as compared to an untreated oxide. To qualitatively assess the dielectric quality, we perform capacitance-voltage (CV) profiling experiments on test-metal-oxide-semiconductor-capacitor devices (MOSCAP), as described in Fig. S4a. The MOSCAPs consist of a material stack resembling that of the qubit devices, but with the difference of using a less resistive heavily p-doped Si substrate to facilitate the capacitance measurements. A DC voltage V_{G} from a DAC (Basel Precision Instruments SP927) is combined with an AC voltage V_{AC} generated by a lock-in amplifier (Stanford Research Systems SR830) and connected to the metal contact of a MOSCAP with a needle prober. The other needle is placed on a region with the exposed p-doped Si substrate and connected to an IV converter (Basel Precision Instruments SP983c), which is then fed back to the lock-in amplifier. The capacitance is calculated from:

$$C = \frac{I_{AC}^{Y}}{2\pi f V_{AC}} \quad , \tag{5}$$

where I_{AC}^{Y} is the measured out-of-phase component of the current signal, and f the lock-in frequency. Upon measuring the CV-curves of the untreated MOSCAP devices, they are annealed in a rapid thermal annealing oven (MBE-Komponenten GmbH AO500). The CV-curves of the devices annealed at different temperatures are shown in Fig. S4b for increasing duration or temperature. The hysteretic behavior of the curves observed in Fig. S4b can be attributed to undesired interface charge traps between the semiconductor and the oxide [10]. This feature is used as a crude indicator for the oxide quality. Subsequent annealing runs significantly reduce the level of the observed hysteresis and are thus associated with an improvement of the dielectric quality. We note that temperatures beyond 300° C were not tested to prevent damage to the Ti/Pd bottom gates of the devices. From 400° C onwards, the bottom gates would show strong signs of deformation.

In summary, we attribute the reduction of hysteresis observed in the CV-curves taken after a 300° C annealing step, to a qualitative improvement of the interface between the p-type substrate and the Al_2O3 oxide. A more thorough analysis would require to also test the effect of annealing on undoped substrate along with performing measurements at cryogenic temperatures. A further limitation is posed by directly probing the chip surface rather than fabricating an ohmic contact to the doped Si substrate, leading to gate voltage offsets due to the needle-semiconductor contact-interface. To investigate any effects of the annealed ALD oxide on qubit coherence, we compare $T_2{}^*$ and T_2^{Hahn} measured in the annealed device (described in the main text) with the values in an unannealed device, whose measured data are overlaid in Fig. S4c and S4d. We note that for the given bias triangle in the unannealed qubit device, no dependence of the qubit coherence on the center gate voltage was observed. Further, no clear difference in coherence times can be observed between both devices, indicating that annealing of the ALD oxide layer did not noticeably improve the qubit quality. We therefore suspect the main source of charge noise to be the native Silicon oxide on the nanowire shell.

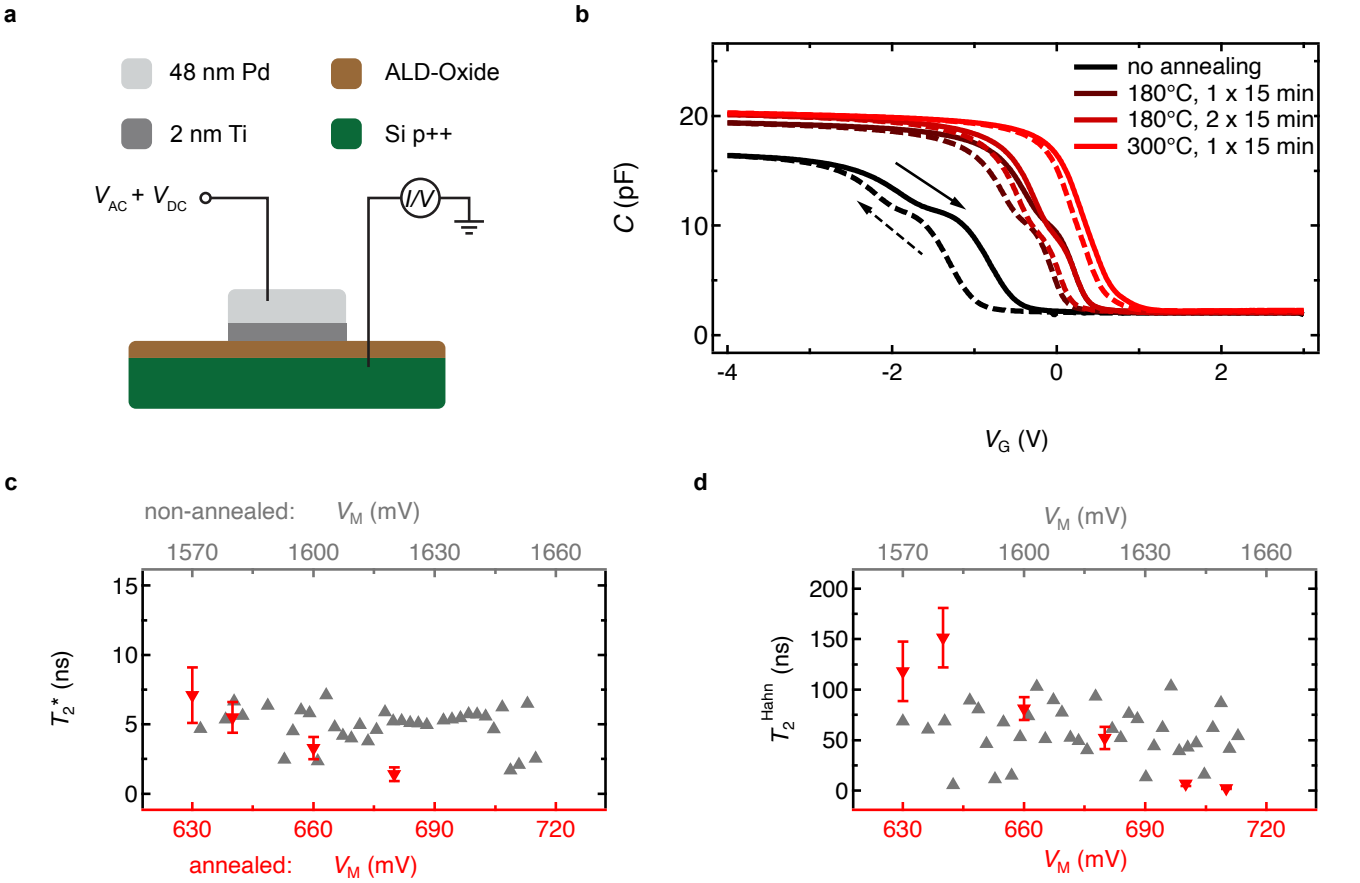

FIG. S4. **Impact of gate dielectric quality on qubit coherence. a,** Schematic of the MOSCAP used for CV profiling. The device consists of a heavily p-doped Si-substrate covered by ~ 24 nm of ALD- oxide grown on top of the native Si-oxide of the substrate. The top electrode is defined by an 80 μm × 80 μm Ti/Pd square. **b,** CV-curves of a MOSCAP taken as a reference prior to (black), and after subsequent annealing runs. The temperatures and durations are indicated in the legend. The sweep directions are indicated by the arrows. **c,** Measured values of the Ramsey free evolution time T_2^* as a function of gate voltage V_M for the non-annealed device (grey) and the annealed device (red). **d,** Same as c but measuring the free evolution time of a Hahn-Echo experiment T_2^{Hahn}.

S5. ESTIMATION OF g-TENSOR MODULATED CONTRIBUTION TO f_R

To first order a periodic voltage fluctuation dV_{RP} on the driving gate RP, will give rise to a gtm-EDSR contribution of magnitude [11],

$$f_R^{gtm}(V) = \frac{\eta}{2} \frac{\partial g(V)}{\partial V_{RP}} \frac{\mu_B}{h} B\, V_{MW} \quad , \tag{6}$$

where V_{MW} is the amplitude of the microwave voltage applied to gate RP, $\partial g/\partial V_{RP}$ is the response of the g-factor to a variation V_{RP}, μ_B Bohr's magneton, h Planck's constant, B is the magnetic field amplitude at the qubit resonance and η is an efficiency accounting for the distance from the driving gate to the assumed qubit location over gate LP. The applied microwave voltage arriving at the sample is $V_{MW} = 7.8$ mV and was obtained from a power calibration. To estimate the efficiency η, we estimate the horizontal and vertical distance of the expected qubit location relative to the driving gate, $d_{hor} = 100$ nm and $d_{vert} = 30$ nm (accounting for ~ 20 nm of dielectric and the NW radius of 10 nm). This roughly results in $\eta \approx 30\%$.

As explained in Sec. S3 $\partial g/\partial V_i$ provides solely an upper bound to the perpendicular component relevant for the g-modulated drive. Based on this estimate, datapoints with contributions to the measured Rabi frequencies above $f_R^{gtm}/f_R \geq 15\%$ of the measured value of f_R are considered significantly affected by g-tensor modulation and were excluded from the fit in Fig. 2g of the main text. The calculated percentages of f_R^{gtm}/f_R are shown in Fig. S5.

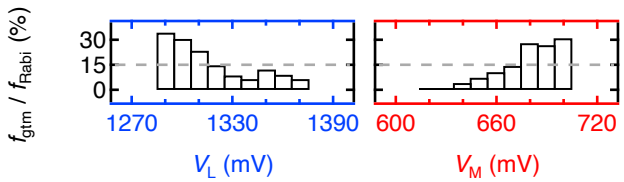

FIG. S5. **Ratio of f_R^{gtm}/f_R.** Calculated contribution to f_R coming from gtm-EDSR represented as the bars. The dashed line corresponds to 15% which was used as our threshold for classification.

S6. EFFECT OF β ON COMPUTED AND MEASURED DECOHERENCE RATES

The best fit of the Hahn-decays was obtained for $\beta = 0$. We further note that the qualitative feature of the coherence sweet spot is robust with respect to the choice of β as seen in Figs. S6a-d. The point at $V_L = 1330$ mV shows some stronger dependence on the choice of noise exponent as opposed to the other points which we explain in the following. Overall, the nature of transport measurements performed in this work, sets an upper bound to the free evolution time τ of the Hahn measurements. If each hole loaded into the double dot were to be measured with efficiency $\eta = 1$, we would expect the maximum possible current e/t_{cycle}, where e is the elementary charge and $t_{\mathrm{cycle}} = 2 \times (t_\pi + 2t_{\pi/2} + 2\tau)$, which yields $e/t_{\mathrm{cycle}} \approx 1$ pA for $t_{\mathrm{cycle}} \approx 150$ ns. The leakage currents of our experiments however correspond to efficiencies on the order of $\eta_{\mathrm{meas}} \approx 0.1$. This inefficiency can be attributed to co-tunneling events, the inefficient loading of the double dot due to the elevated temperature of operation of 1.5 K or random variations of the device behaviour after a thermal cycle of the device. In the case of $V_L = 1330$ mV, the highest τ used did not suffice to observe a significant characteristic decay of the Hahn-echo. Further increasing of τ would have lead to transport currents which are too small to measure. Therefore in this case, the fit was more sensitive on the choice of β.

For the models of decoherence rates for non-zero β, we use the generic expression as derived in the Supplementary Information of [12]:

$$\frac{1}{T_2^{\mathrm{Hahn}}} = 2\pi \left(C_\beta f_0^\beta \sum_i \left(\frac{\partial g}{\partial V_i} S_G \right)^2 \right)^{\frac{1}{\beta+1}} \quad , \tag{7}$$

with $C_\beta = 2\sin(\frac{\beta\pi}{2})(2^{1-\beta} - 1)\Gamma(-1-\beta)$, Γ, the Gamma function Γ, and $S_G = S_G(f_0/f)$ is the noise spectral density at reference frequency $f_0 \approx 12.5$ MHz for our measurements.

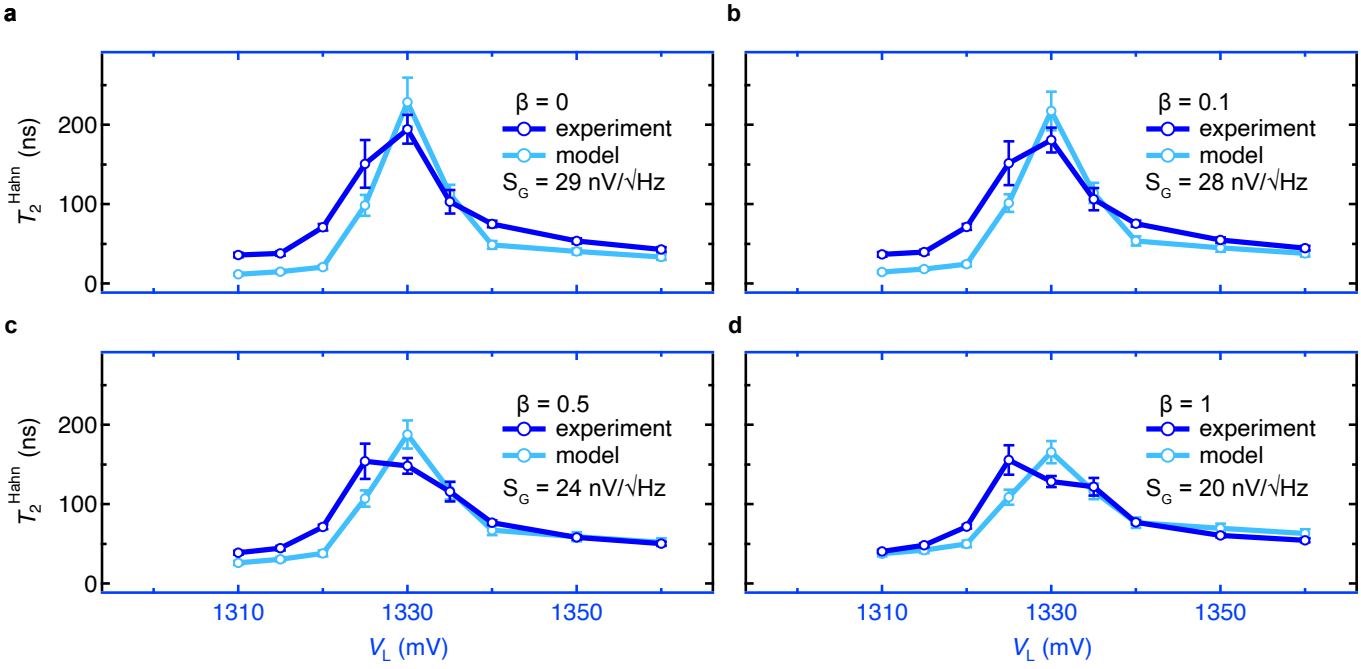

FIG. S6. **Analysis of the experimental Hahn-echo data and model for $\beta \in \{0,\ 0.1,\ 0.5,\ 1\}$. a,** Identical traces as presented in Fig. 3a of the main text for $\beta = 0$. **b-d,** Traces for $\beta \in \{0.1,\ 0.5,\ 1\}$. All models for non-zero β were computed using Eq. 7.

S7. 2D VOLTAGE MAPS OF f_R AND T_2^{Hahn}

To emphasize the overlap of maxima of T_2^{Hahn} and f_R, we present in Fig. S7a the 2D-voltage dependence of T_2^{Hahn}, which was already introduced in the main text, as well as the 2D-voltage dependence of f_R in Fig. S7b, of which only the contours were presented in the main text. Finally, Fig. S7c is obtained by overlaying the contours of the interpolated background of Fig. S7b on top of Fig. S7a.

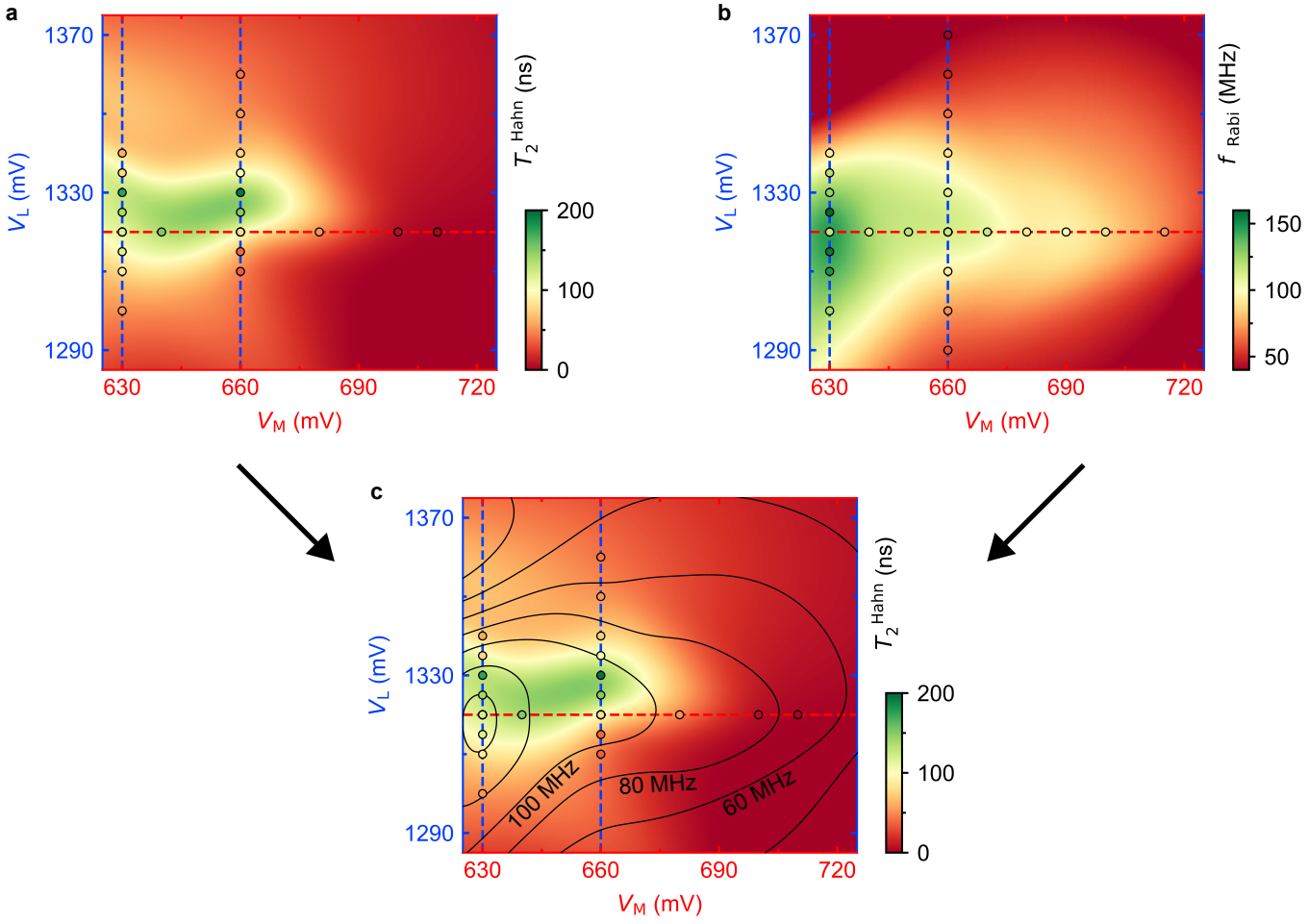

FIG. S7. **2D maps of the FACTOR as a function of V_L and V_M. a,** 2D voltage space showing T_2^{Hahn} as a function of gate voltages V_M and V_L. The filled circles represent the measured coherence times T_2^{Hahn}. The background is obtained by a Gaussian process interpolation and serves as a guide to the eye. **b,** Analogous to panel a, but for f_R. **c,** Shows the contours of f_R from panel b overlaid on the plot of T_2^{Hahn} in panel a, to emphasize the overlap of both maxima.

[1] C. Kloeffel, M. Trif, P. Stano, and D. Loss, Physical Review B **88**, 241405 (2013).
[2] S. Bosco, M. Benito, C. Adelsberger, and D. Loss, Physical Review B **104**, 115425 (2021).
[3] V. N. Golovach, M. Borhani, and D. Loss, Physical Review B **74**, 165319 (2006).
[4] A. Crippa, R. Maurand, L. Bourdet, D. Kotekar-Patil, A. Amisse, X. Jehl, M. Sanquer, R. Laviéville, H. Bohuslavskyi, L. Hutin, S. Barraud, M. Vinet, Y.-M. Niquet, and S. D. Franceschi, Physical Review Letters **120**, 137702 (2018).
[5] S. Bosco, P. Scarlino, J. Klinovaja, and D. Loss, Physical Review Letters **129**, 066801 (2022).
[6] S. Bosco, S. Geyer, L. C. Camenzind, R. S. Eggli, A. Fuhrer, R. J. Warburton, D. M. Zumbühl, J. C. Egues, A. V. Kuhlmann, and D. Loss, Physical Review Letters **131**, 197001 (2023).
[7] J. Yoneda, K. Takeda, T. Otsuka, T. Nakajima, M. R. Delbecq, G. Allison, T. Honda, T. Kodera, S. Oda, Y. Hoshi, N. Usami, K. M. Itoh, and S. Tarucha, Nature Nanotechnology **13**, 102 (2017).
[8] D. Culcer, X. Hu, and S. Das Sarma, Applied Physics Letters **95** (2009), 10.1063/1.3194778.
[9] D. K. Schroder, "Semiconductor material and device characterization," (2005).
[10] L. Massai, B. Hetényi, M. Mergenthaler, F. J. Schupp, L. Sommer, S. Paredes, S. W. Bedell, P. Harvey-Collard, G. Salis, A. Fuhrer, and N. W. Hendrickx, arXiv (2023), 10.48550/ARXIV.2310.05902, arXiv:2310.05902 [cond-mat.mes-hall].
[11] V. P. Michal, J. C. Abadillo-Uriel, S. Zihlmann, R. Maurand, Y.-M. Niquet, and M. Filippone, Physical Review B **107**, l041303 (2023).
[12] N. Piot, B. Brun, V. Schmitt, S. Zihlmann, V. P. Michal, A. Apra, J. C. Abadillo-Uriel, X. Jehl, B. Bertrand, H. Niebojewski, L. Hutin, M. Vinet, M. Urdampilleta, T. Meunier, Y.-M. Niquet, R. Maurand, and S. D. Franceschi, Nature Nanotechnology **17**, 1072 (2022).